

A Fully Convolutional Network for Rectal Cancer Segmentation

Joohyung Lee, Ji Eun Oh, Min Ju Kim, Bo Yun Hur, and Dae Kyung Sohn

Abstract—In preoperative imaging, the demarcation of rectal cancer forms an important basis for various tasks including prediction, staging, and treatment planning. The aim of this study is to develop a fully automatic method to segment rectal cancer with axial T2-weighted magnetic resonance images. In order to improve the performance, the network was supplemented with the rectum segmentation task as well, which is also clinically informative. Moreover, we propose an assessment method based on bias-variance decomposition to visualize and measure the regional model robustness of a segmentation network. In addition, we implement an augmentation method enabled by the fully convolutional nature of the network, showing that it improves segmentation performance and reduces training time. Our proposed method is computationally efficient compared to the previous studies regarding rectal cancer segmentation. It also shows high accuracy in rectum segmentation, for which no previous studies exist. We conclude that rectum information improves the training of the rectal cancer segmentation model, especially model variance.

I. INTRODUCTION

Colorectal cancer is the third most common cancer, globally, and the second leading cause of cancer mortality [1]. Specifically, colorectal cancer was the most commonly diagnosed cancer in Korea in 2017, with 27,837 new cases [2]. The global burden of colorectal cancer is rising fast and is expected to increase by 60% by 2030 [3].

The Union for International Cancer Control's TNM Classification of Malignant Tumors (8th edition) categorizes rectal cancer as a tumor starting in the rectum, i.e., the last 12 centimeters of the colon [4]. Furthermore, the T-category of rectal cancer pathologically classifies its progression by the degree of tumor invasion to the rectal wall. In MR images, the T-category can be determined by the relative location of the tumor and the rectal wall [5]. Since the current treatment guidelines for rectal cancer recommend different treatments depending on the T-category, accurate segmentation of rectum and rectal cancer is crucial. However, in practice, radiologists manually locate rectum and rectal cancer using MR images so as to determine the T-category. Manual localization is time-consuming, and a reliable auto-segmentation system is needed [6].

In recent years, deep learning has improved the state-of-the-art in various fields related to computer vision [7]. Its wide applicability derives from its ability to find complex structures in high-dimensional data. Specifically, the ability of deep learning to learn a complex representation of images was enhanced by the introduction of convolutional neural networks (CNNs) consisting of two different layers, the convolution layer and the pooling layer. By convoluting adjacent values, which are often highly correlated, a CNN detects the local motifs of the previous layer. Furthermore, its pooling layer reduces the dimension of the representation and provides robustness against small shifts or noise while at the same time increasing the receptive field. Through convolution and pooling layers, a CNN can learn image representation hierarchically, combining lower level features to create higher-level features [8]. Moreover, further improvements in CNN architectures using large image data, such as the application of residual connection, were recently developed [9-13].

Deep learning has also proved its applicability in various medical image analysis tasks, including medical image segmentation [14]. Specifically, Ronneberger et al. have introduced the U-Net by implementing a VGG-Net-like encoder together with a mirrored decoder with a convolution transpose layer [15]. Milletari et al. have extended the U-Net to 3D data and introduced the Dice similarity coefficient-based loss function for the segmentation of the prostate volume in MRI [16]. However, automation of medical image analysis is challenging due to the inherent complexity of the images and the extensive variation between patients [17]. Such complexity and large variability within data call for a model with large capacity, able to discover more intricate structures in the data. However, models with high capacity can suffer from overfitting, unless trained with many samples satisfying the i.i.d. assumption [18].

Unfortunately, in practice, less abundant image data are available in the medical field than in other fields. As a result, overfitting can be a problem in building a network for medical image analysis.

Various attempts have been proposed to moderate overfitting in deep learning, such as batch normalization, drop-out, max-out, image augmentation, image normalization, etc.[19-21]. In addition to these approaches, multi-task learning (MTL) is known to reduce the risk of overfitting [18, 22]. By adding an additional task, the parameters of the model are optimized towards values that can explain the variation observed in both tasks, reducing the risk of overfitting with respect to the original task and thus enhancing model robustness. In case of deep neural network, the shared portion of the network can be constrained towards values with better generalization ability, if the additional task can provide information relevant to the original task. As a result, sharing a network can reduce the risk of overfitting and allow the model to achieve better generalization and robustness if the additional task is related to the original one.

Overfitting is often explained with the bias-variance decomposition of the expected loss [18]. Since overfitting is usually related to high variance, i.e., low model robustness, measuring model variance can be beneficial. Although the mean squared error is often used to explain the trade-off, due to its easy decomposition, the unified theorem for bias-variance decomposition also enables arbitrary loss functions to be decomposed into noise, bias, and variance [23].

In this paper, we developed a fully automatic multi-region segmentation method to segment rectal cancer together with the rectum. We assumed that learning about the rectum would benefit the learning of rectal cancer, especially in terms of overfitting. Such an assumption was based on considering their inherent geometrical correlation as well as the comparatively more consistent shape of the rectum. Specifically, since rectal cancer grows from the rectum area, it is mostly located inside the rectum [5]. In our study, since our dataset only includes images that clearly reflect either T2- or T3-stage rectal cancer, rectal cancer is always found along the rectum wall, which strengthens our assumption that rectum information can benefit rectal cancer segmentation due to their geometrical correlation [4]. “Tumor” represents rectal cancer throughout this paper unless stated otherwise.

The main contributions of this work are the following:

1. Unlike previous method, which classifies the center pixel of an image patch, we propose an encoder-decoder type segmentation network that uses the whole MR image[6]. Our method is thus computationally efficient and can benefit current clinical procedures for treatment planning.
2. We show that adding a rectum segmentation task can improve the performance of rectal cancer segmentation especially in model variance.
3. We propose a method to visualize and assess the regional robustness of an image segmentation network by applying the bias-variance decomposition at the single-pixel scale.
4. We assess the efficacy of the augmentation method based on image resizing, which can improve the segmentation performance, especially when trained with images of heterogeneous resolution.

II. RELATED WORKS

To the best of our knowledge, no study has suggested a rectum auto-segmentation system using MR images. Regarding rectal cancer segmentation systems using MR images, Trebeschi et al. have proposed a patch-based training of a CNN model using both T2-weighted images and diffusion-weighted images (DWI) from MRI [6]. It has to be noted that the network classifies image patches using a fully-connected layer and decides the class of the center pixel of an input image patch, which is computationally less efficient than a fully-convolutional approach [24]. The authors sampled more patches from the regions with intensity values similar to those of rectal cancer, and included a post-processing step that only maintains the largest positive area (rectal cancer) to remove false positive pixels. The system can be inappropriate when more than one tumor exists in an image. Moreover, since the 135 images were divided into training, validation, and test set without cross-validation, their evaluation could have suffered from data selection bias. In addition, we are not aware of any previous study implementing bias-variance decomposition in the field of image segmentation.

III. MATERIALS AND METHODS

A. Data Preparation

The experiments were performed using MR images of 1,813 patients with rectal cancer, obtained between September 2004 and June 2016 at the National Cancer Center of South Korea. Out of 1,813 patients, 457 were selected after disregarding the cases with at least one of the following properties: preoperative chemo-radiation, incomplete pathologic stage information, disagreement between MR and pathologic stages, pathologic stage T1 or T4, tumors

located more than 13 cm or less than 3 cm from the anal verge, or the application of either clipping or stents. All studies were conducted according to the principles of the Declaration of Helsinki, and the protocol was approved by the Institutional Review Board of our institution (NCC2017-0031).

Rectal MR examinations were performed with one of four 3T or 1.5T superconducting systems (namely, Achieva 3.0T (n = 233) and Achieva 3.0T TX (n = 131), Philips Healthcare, Cleveland, OH, USA; Signa HDX 3.0T (n = 19) and Genesis Signa 1.5T (n = 74), GE Healthcare, Milwaukee, WI, USA) using pelvic phased-array coils. Among the various MR imaging sequences, this experiment evaluated axial T2-weighted fast-spin echo images.

Among approximately 30 image slices available per patient, one or two were selected to create our dataset. The selected images clearly reflected the T-category of the patient by showing the rectum with the clear appearance of either T2 or T3 rectal cancer. Two gastrointestinal clinical specialists were involved not only in selecting 907 image slices from the 457 cases, but also in manually segmenting both rectum and rectal cancer for all the images. Specifically, one specialist drew the boundary, and the other specialist confirmed the segmentation outcome. The manual segmentation results were used as our ground truth.

Finally, the 907 images were divided into ten folds for 10-fold cross-validation as well as for bias-variance assessment. All images from the same patient were assigned to the same fold. For bias-variance assessment, we set apart the 10th fold as our test set and produced nine training sets, as in a 9-fold cross-validation procedure. Note that we did not use the validation set like in 9-fold cross-validation, but only used the test set for bias-variance assessment, resulting in nine different prediction maps for every test image.

B. Preprocessing

Both image intensity range normalization and histogram equalization were applied in order to improve image contrast and generalization [25]. As a normalization step, both 90% of the maximum and the minimum intensity value from the overall image slices of a patient were used to reduce the image depth from 12-bit to 8-bit. Contrast-limited adaptive histogram equalization was also applied to enhance the contrast as well as to reduce the effects of magnetic bias [26, 27]. As shown in Figure 1, an image with a high-intensity artifact region, which decreases the overall image contrast, became more interpretable after preprocessing. In addition, all images were resized to 256×256 , after histogram equalization, since the image-size of the original MR images varies from 512×512 to 1056×1056 depending on the MR scanner.

During optimization, all training data underwent random augmentation including adjusting the contrast, brightness, and sharpness followed by rotation, flipping (left and right), and cropping (maximum 10% from the edge and preserving the square shape). On the other hand, neither the validation nor the test data were augmented.

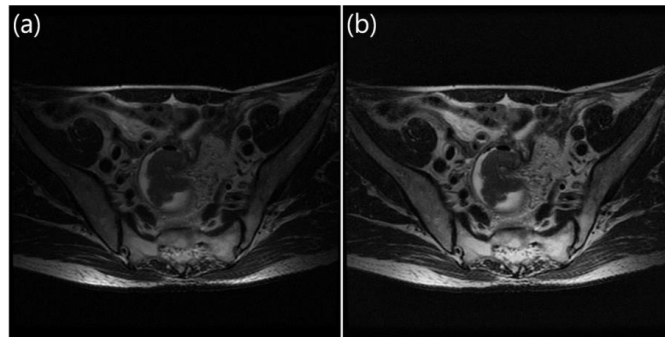


Fig. 1. Sample image before and after preprocessing. (a) Original image; (b) preprocessed image.

C. Our fully convolutional neural network approach

We implemented an encoder-decoder type segmentation network for the fully convolutional multi-region segmentation network. To segment both rectum and rectal cancer simultaneously, two task-specific 1×1 convolution layers were implemented in parallel, as shown in Figure 2. Moreover, because rectum and rectal cancer can overlap

each other, we did not map each pixel to a multinomial distribution through the softmax function, but implemented the logistic sigmoid function for both classes.

The network involves seven convolution blocks between pooling layers and convolution transpose. To such seven blocks, we applied one of three different block types, shown in Figure 3, and compared their respective performance. In Figure 3, note that convolution block1 involves no residual skip connection, whereas both convolution block2 and convolution block3 use residual skip connections in different ways. For both block2 and block3, we adopted a pre-activation policy for every convolution layer [12]. Moreover, the very first convolution layer of the network involves 40 3×3 filters. The number of filters of the encoder portion is doubled after each convolution block like in VGG-Net or U-Net [10, 15]. The decoder portion is a mirrored version of the encoder, so that the number of filters is halved after each convolution block. More specifically, the doubling or halving of the number of filters is performed by the first convolution in each block.

All filter weights were initialized using the normal distribution sampling method suggested by He et al., except for the convolution transpose filter which was initialized using the uniform distribution sampling method suggested by Glorot and Bengio [28, 29]. The Adam optimization algorithm was implemented to stochastically optimize the parameters with a mini-batch size of 20 [30]. Due to the preponderance of negative pixels, we implemented the Dice Similarity Coefficient (DSC) based loss function suggested by Milletari et al. as our optimization objective function, which is defined as follows [16]:

$$D = \frac{-2 \sum_i^N p_i g_i}{\sum_i^N p_i^2 + \sum_i^N g_i^2}$$

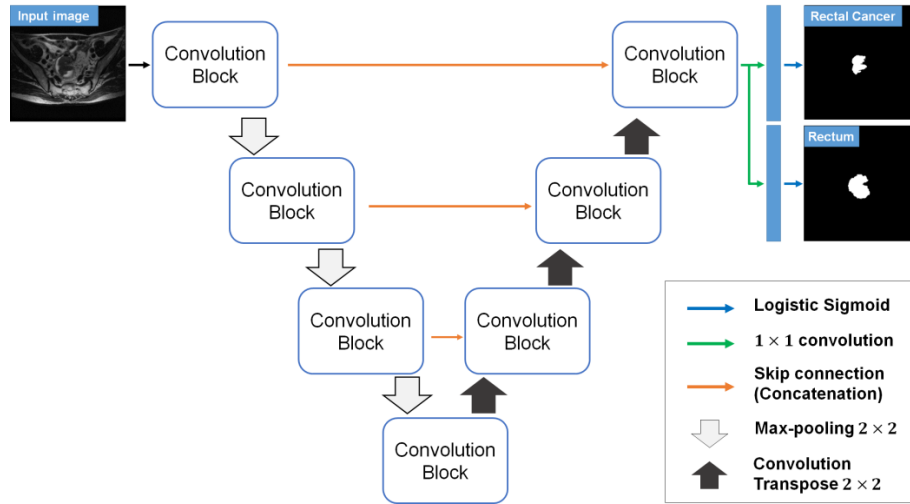


Fig. 2. Fully convolutional network to segment both rectum and rectal cancer simultaneously.

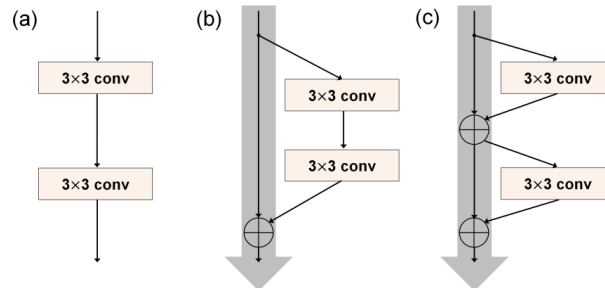


Fig. 3. Three convolution blocks for our network backbone. (a) Convolution block1, (b) convolution block2, and (c) convolution block3.

D. Performance evaluation

Conventional 10-fold cross-validation was implemented in order to compare the performance of different networks. Furthermore, due to the preponderance of negative regions, we used also the DSC as our metric to assess the similarity between the ground truth map and the prediction map, in addition to the conventional sensitivity and specificity. The DSC is defined as follows:

$$DSC(A, B) = \frac{2|A \cap B|}{|A| + |B|}$$

E. Bias-variance assessment

To assess how learning about the rectum affects the learning of rectal cancer, especially concerning overfitting, we measured the variance, the bias, and the expected loss of the prediction map per pixel generated by the multi-region segmentation network (MRSN) and the single-region segmentation network (SRSN) according to the unified definition [23]. However, the unified bias-variance decomposition suggested by Domingos involves an assumption that the true value t is a nondeterministic function of the input x . As a result, the decomposition is done for the expected loss not only over the distribution of the training set D , but also over the distribution of the true value t . According to the unified definition, the decomposition can be described as follows:

$$\begin{aligned} E_{D,t}[L(y^*, y)] &= c_1 E_t[L(t, y^*)] + L(y^*, y_m) + c_2 E_D[L(y_m, y)] \\ &= c_1 N(x) + B(x) + c_2 V(x) \end{aligned}$$

$N(x)$, $B(x)$, and $V(x)$ represent the noise, the bias of a learner, and the variance of a learner on sample x , respectively. Moreover, y^* and y are the optimal prediction and the prediction of the learner, respectively. L is an arbitrary loss function (zero-one loss for our case) and $c_2 = 1$ if $y_m = y^*$ (unbiased prediction), while $c_2 = -1$ if the prediction is biased. y_m is the main prediction, defined as follows:

$$y_m^{L,D} = \operatorname{argmin}_{y'} E_D[L(y, y')]$$

Since we decompose the expected loss of an arbitrary pixel i , y_m will be the most frequent prediction for such pixel, and having nine different prediction maps (from nine different training sets), there will be no ties. Moreover, the proposed decomposition can be simplified as shown below considering that 1) we have a deterministic ground truth for every test sample, and 2) we decompose the loss at an arbitrary pixel i :

$$\begin{aligned} E_D[L(y^*(i), y(i))] &= L(y^*(i), y_m(i)) + c_2 E_D[L(y_m(i), y(i))] \\ &= B_i(x) + c_2 V_i(x) \end{aligned}$$

Finally, since the decomposition is performed pixel-wise, we averaged the bias and variance over all pixels in an image as follows:

$$\begin{aligned} E_{D,i}[L(y^*(i), y(i))] &= E_i[L(y^*(i), y_m(i))] + c_2 E_{D,i}[L(y_m(i), y(i))] \\ &= E_i[B_i(x)] + E_i[c_2 V_i(x)] \end{aligned}$$

Since the variance negatively (positively) affects the expected loss of a biased (unbiased) pixel, we also averaged the variance of biased and unbiased pixels separately.

In summary, we measured the bias, variance, and expected loss per pixel in order to visualize and compare the regional robustness of the rectal cancer prediction map by MRSN and SRSN. We also averaged these values to measure the expected value per pixel. Furthermore, these values were also averaged over positive (tumor) regions only, considering the large number of less informative pixels, such as non-body pixels where both bias and variance are mostly zero.

F. Image size augmentation

Since our dataset consisted of images with various resolutions, we aimed to enhance the robustness of our model with respect to varying resolution. To this purpose, we implemented and assessed the efficacy of the augmentation method, which randomly varies the image size of a mini-batch. Although we exploited the nature of the fully convolutional network, which can accept images of various sizes as its input, we had to synchronize the size of all images within a mini-batch. Specifically, we randomly resized every mini-batch around 256x256 (from 192x192 to 288x288) considering that the image size of our validation set is fixed to 256x256. Images were kept square as all original images are square.

IV. RESULTS AND DISCUSSION

A. Network backbone selection

Table 1 presents the validation performance of the 10-fold cross-validation comparing the three different network backbones. As shown in the table, Block 3 (convolution block3 in Figure 3) scored the highest DSC for both segmentation tasks (rectal cancer and rectum), and thus was selected as our network backbone. Moreover, Block 3 was also trained faster than the other two blocks (Block 1 was 1.46 times slower, and Block 2 was 1.04 times slower). Note that the blocks with residual connections were trained faster than those without connections.

B. Comparing multi-region and single-region segmentation networks

Two separate SRSNs for rectum and rectal cancer segmentation were trained with the selected network backbone. Figure 4 shows an example of the learning progression of MRSN and SRSNs. The performance of SRSNs in both rectum and rectal cancer segmentation were compared with the corresponding performance of MRSN via 10-fold cross-validation, as shown in Table 2. In addition to better segmentation performance, the training of MRSN networks (10-fold cross-validation) took less time than that of the tumor and rectum SRSNs, on average, by a factor of 0.96 and 0.81, respectively.

Statistical analysis was performed in order to validate the comparisons in Table 2. Significant differences (paired t-test) between MRSN and SRSN were observed in tumor DSC ($p = 0.02$) as well as tumor sensitivity ($p = 0.01$). No other quantities were significantly different between MRSN and SRSN.

C. Bias-variance assessment

In section 4.2, we statistically confirmed that the MRSN outperformed the SRSN in rectal cancer segmentation,

TABLE I
PERFORMANCE COMPARISON OF THREE DIFFERENT NETWORK BACKBONES

	DSC		Sensitivity		Specificity	
	Tumor	Rectum	Tumor	Rectum	Tumor	Rectum
Block 1	0.718 ± 0.201	0.935 ± 0.090	0.736 ± 0.225	0.932 ± 0.108	0.999 ± 0.002	0.999 ± 0.002
Block 2	0.722 ± 0.204	0.936 ± 0.092	0.741 ± 0.230	0.937 ± 0.105	0.999 ± 0.002	0.999 ± 0.002
Block 3	0.732 ± 0.195	0.938 ± 0.079	0.755 ± 0.221	0.936 ± 0.104	0.999 ± 0.002	0.999 ± 0.002

All quantities are expressed as mean \pm standard deviation and were obtained through 10-fold cross-validation.

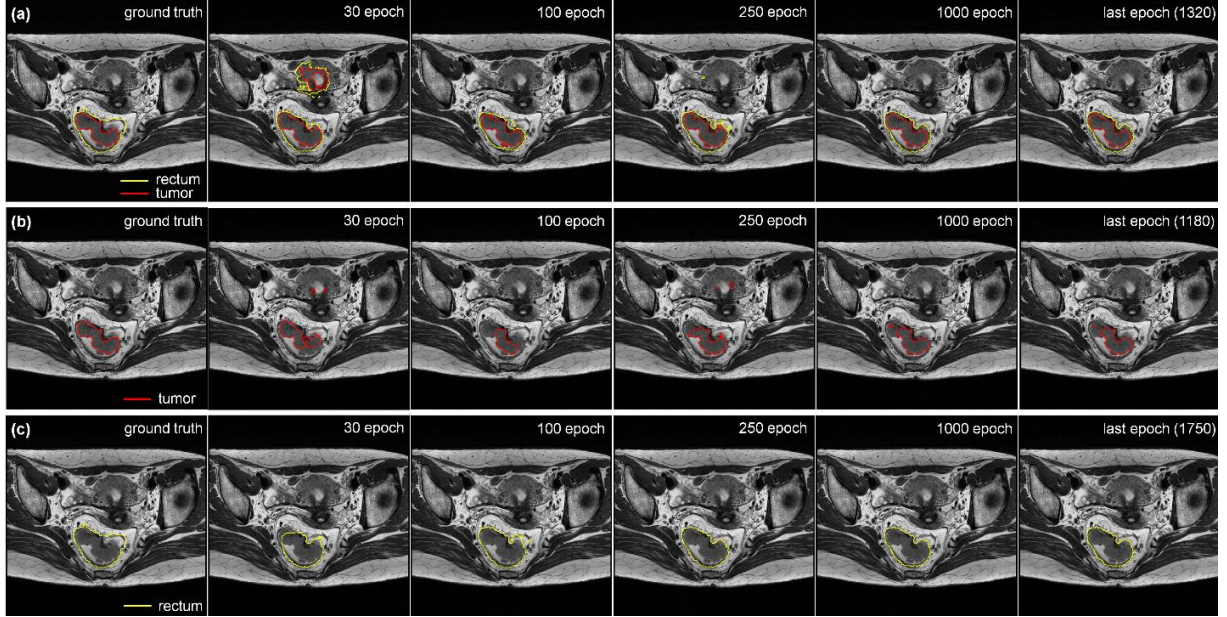


Fig. 4. MRSN and SRSN learning process. Panels (a), (b), and (c) show the learning progress of the MRSN, SRSN (tumor), and SRSN (rectum), respectively. The 6th column displays the prediction map of the last epoch.

In order to visualize how and in which region learning about the rectum improved the learning of rectal cancer, especially in terms of model robustness, our test set was predicted by the nine different models from nine different training sets. Figure 5 shows an example of the nine different prediction maps generated by SRSN and MRSN used to obtain bias and variance maps.

As can be seen in the figure, the SRSN network made abnormal positive predictions above the normal prediction region in prediction maps 5 and 6. Such regional model variance calls for a visualization method to assess the regional model robustness.

Figure 6 presents three examples of bias, variance, expected loss, and ground truth maps for rectal cancer prediction overlaid on the input MR image. The variance map suggests a regional model robustness of the rectal cancer segmentation network. Moreover, combined with the bias map, the variance map creates the expected loss map, which gives a notion of how the variance affects the expected loss. Because rectal cancer occupies only a small portion of the image, we cropped the image according to the yellow box in column (d), only for visualization purposes. The yellow arrows indicate notable differences between SRSN and MRSN.

TABLE II
PERFORMANCE COMPARISON BETWEEN SRSN AND MRSN

	DSC		Sensitivity		Specificity	
	Tumor	Rectum	Tumor	Rectum	Tumor	Rectum
MRSN	0.732 ± 0.195	0.938 ± 0.079	0.755 ± 0.221	0.936 ± 0.104	0.999 ± 0.002	0.999 ± 0.002
SRSN	0.723 ± 0.204	0.940 ± 0.088	0.743 ± 0.232	0.938 ± 0.107	0.999 ± 0.002	0.999 ± 0.002

All quantities are expressed as mean \pm standard deviation and were obtained through 10-fold cross-validation. Quantities shown in bold are significantly different ($p < 0.05$) between MTL and STL.

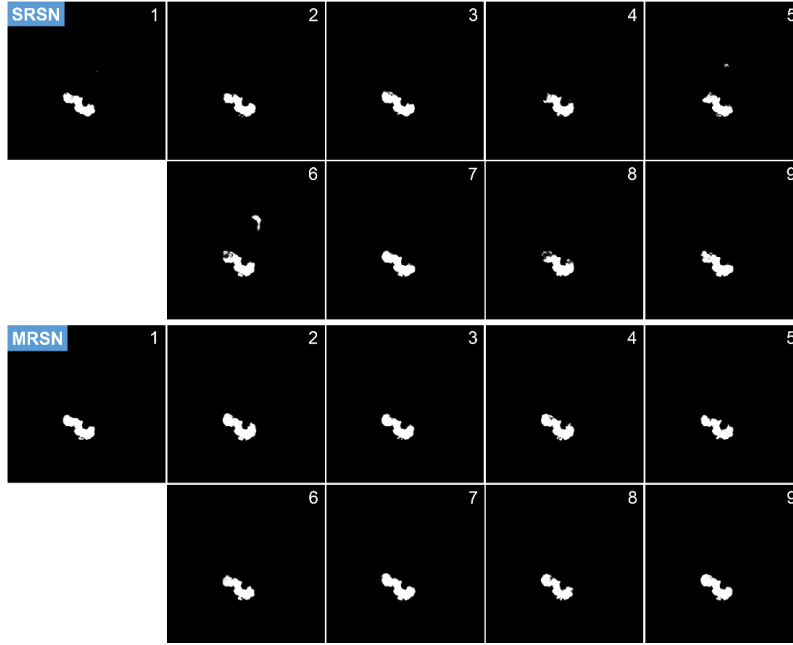


Fig. 5. Nine rectal cancer prediction maps on a test sample. The first two rows are the maps predicted by SRSN whereas the third and fourth rows are derived from MRSN. The SRSN and MRSN networks share training data only if the prediction number (located at the top right corner of each map) is the same. Each map is generated by one of the nine different training sets, as described in section 3.2.

Most bias and variance occurred at the boundary of the rectal cancer. However, SRSN occasionally showed low robustness at organs other than the rectum, but with similar appearance in MR images. Moreover, within the rectal cancer region, SRSN showed more variance, which is noticeable in particular in the bottommost example in Figure 6.

Furthermore, we measured the average bias ($E[\text{Bias}]$), average variance ($E[\text{Var}_{\text{Total}}]$), and average expected loss ($E[L]$) per image and compared them between SRSN and MRSN. Table 3 shows that learning about the rectum decreased both bias and variance in rectal cancer segmentation, with a statistically significant decrease in variance ($p = 0.0002$). Note that learning about the rectum increased the variance in biased pixels ($E[\text{Var}_{\text{Biased}}]$) in the rectal cancer segmentation model, whereas it significantly reduced the variance of unbiased pixels ($E[\text{Var}_{\text{Unbiased}}]$, $p = 2.78e-5$). Learning about the rectum altered the bias, the variance of biased pixels, and the variance of unbiased pixels in such a way as to reduce the expected loss of rectal cancer segmentation. The expected loss was thus significantly reduced by learning about the rectum ($p = 0.0002$). Note that the variance of biased pixels negatively affects the expected loss.

TABLE III
EXPECTED BIAS, EXPECTED VARIANCE (TOTAL, BIASED, UNBIASED), AND EXPECTED ZERO-ONE LOSS FOR POSITIVE REGION AND WHOLE REGION.

		$E[\text{Bias}]$	$E[\text{Var}_{\text{Total}}]$	$E[\text{Var}_{\text{Biased}}]$	$E[\text{Var}_{\text{Unbiased}}]$	$E[L]$
Positive	SRSN	0.248 ± 0.232	0.093 ± 0.065	0.189 ± 0.089	0.091 ± 0.080	0.272 ± 0.225
	MRSN	0.232 ± 0.232	0.084 ± 0.054	0.200 ± 0.183	0.075 ± 0.058	0.246 ± 0.214
Total	SRSN	0.003 ± 0.004	0.001 ± 0.001	0.180 ± 0.071	0.001 ± 0.001	0.003 ± 0.004
	MRSN	0.003 ± 0.004	0.001 ± 0.001	0.183 ± 0.069	0.001 ± 0.001	0.003 ± 0.004

Quantities shown in bold are significantly different ($p < 0.05$) between MRSN and SRSN.

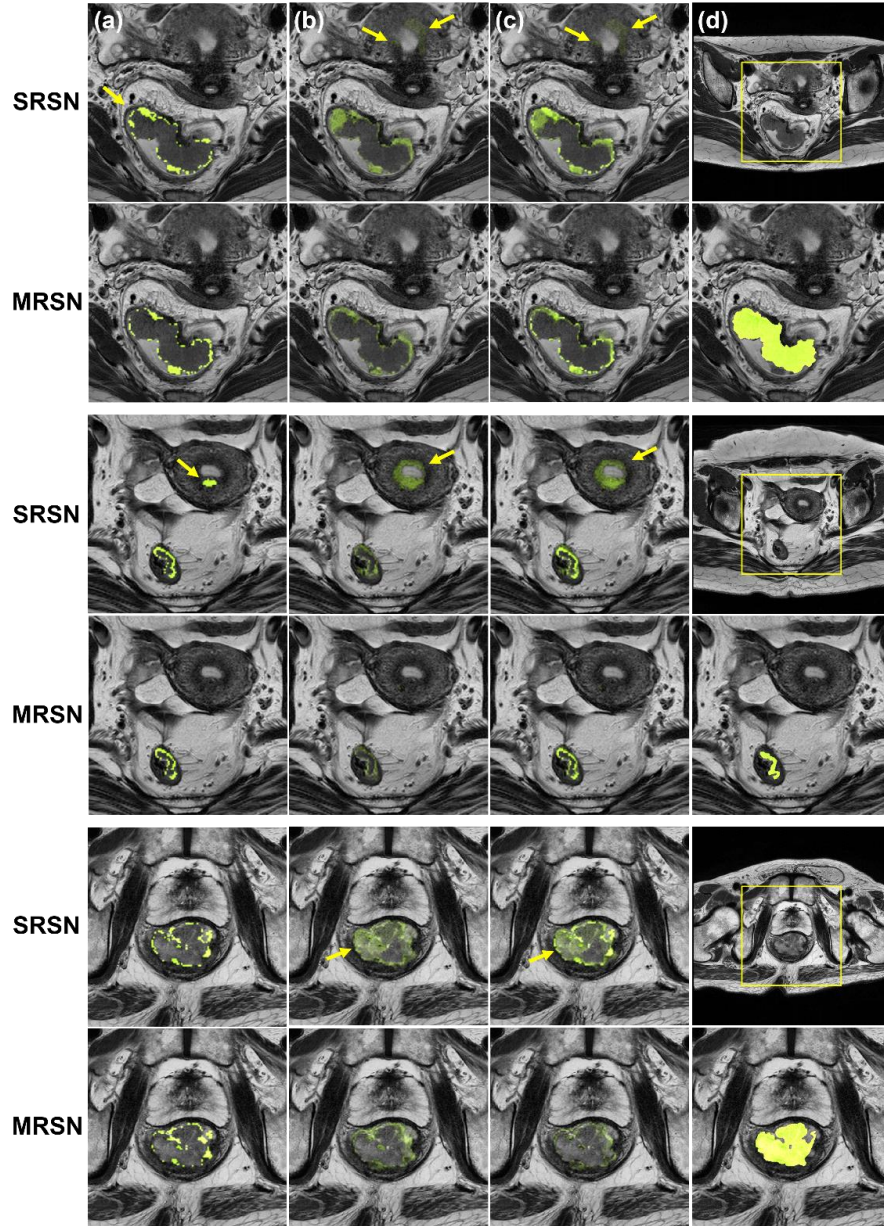


Fig. 6. Three test examples of maps of rectal cancer prediction produced by SRSN and MRSN overlaid with their bias (a), variance (b), and expected loss (c). Column (d) shows the original image with the yellow box indicating the cropping boundary used for visualization purposes, as well as the ground truth. Note that the uppermost example corresponds with that shown in Fig. 5, and the regional variance of the SRSN at other organs is captured by the variance map as well as the expected loss map. Both variance and expected loss are higher if represented with more yellow than green.

D. Image size augmentation

We measured the efficacy of our image size augmentation on MRSN through 10-fold cross-validation. The augmentation improved the performance of both rectum and rectal cancer segmentation, with significant differences in the tumor DSC ($p = 8.84e-5$), rectum DSC ($p = 1.02e-5$), tumor sensitivity ($p = 0.0003$), rectum sensitivity ($p = 0.001$), and rectum specificity ($p = 0.016$). The augmentation also reduced the average training duration by a factor of 0.78.

TABLE IV
PERFORMANCE COMPARISON OF MRSN WITH AND WITHOUT IMAGE SIZE AUGMENTATION.

	DSC		Sensitivity		Specificity	
	Tumor	Rectum	Tumor	Rectum	Tumor	Rectum
MRSN	0.732 ± 0.195	0.938 ± 0.079	0.755 ± 0.221	0.936 ± 0.104	0.999 ± 0.002	0.999 ± 0.002
MRSN-AUG	0.746 ± 0.186	0.944 ± 0.070	0.770 ± 0.214	0.941 ± 0.095	0.999 ± 0.002	0.999 ± 0.002

All quantities are expressed as mean \pm standard deviation and were obtained through 10-fold cross-validation. Quantities shown in bold are significantly different ($p < 0.05$) between MRSN and MRSN-AUG.

V. CONCLUSION

Accurate and fast segmentation of rectal cancer is clinically crucial. Unlike the previous patch-based method, we applied the encoder-decoder network to segment the whole MR image in order to improve the computational efficiency [6, 24]. Moreover, to reduce the model variance, we supplemented the network with rectum segmentation task. As a result, our method scored a DSC of 0.746 and 0.944 in rectal cancer and rectum segmentation, respectively (0.006 seconds to infer both regions from single image).

To this end, unlike the current state-of-the-art method of rectal cancer segmentation, our method does not extract patches from MR image to classify their center pixel, which is computationally inefficient [6, 24]. Instead, our proposed method, by efficiently segmenting both rectum and rectal cancer from the whole image, scored a DSC of 0.746 and 0.944 in rectal cancer and rectum segmentation, respectively. In addition, no previous studies have reported rectum segmentation using axial MR image.

We also propose a method to visualize and assess the regional model robustness of an image segmentation network. By measuring the bias, variance, and expected loss, we concluded that both rectum information and the augmentation procedure that produces multiple image size benefit the training of our rectal cancer segmentation model, especially in terms of model robustness. The assessment procedure we proposed can be especially beneficial in evaluating high capacity models trained with limited number of images, which often suffer from overfitting.

Our method for rectal cancer segmentation is devised in order to improve the model robustness as well as the computational efficiency. Moreover, its accurate rectum region prediction is clinically informative. Our method is expected to expedite the current manual localization procedure performed by radiologists and assist professionals in determining the T-category of rectal cancer for treatment planning.

ACKNOWLEDGMENT

This project was supported by a grant from the National Cancer Center [grant number NCC-1710070]. We kindly thank Sun Ah Cho for her support in data acquisition.

REFERENCES

- [1] A. Bhandari, M. Woodhouse, and S. Gupta, "Colorectal cancer is a leading cause of cancer incidence and mortality among adults younger than 50 years in the USA: a SEER-based analysis with comparison to other young-onset cancers," *J. Invest. Med.*, vol. 65, no. 2, pp. 311-315, 2017.

- [2] K.-W. Jung, Y.-J. Won, C.-M. Oh, H.-J. Kong, D. H. Lee, and K. H. Lee, "Prediction of cancer incidence and mortality in Korea, 2017," *Cancer Res. Treat.*, vol. 49, no. 2, pp. 306-312, 2017.
- [3] M. Arnold, M. S. Sierra, M. Laversanne, I. Soerjomataram, A. Jemal, and F. Bray, "Global patterns and trends in colorectal cancer incidence and mortality," *Gut*, vol. 66, no. 4, pp. 683-691, 2017.
- [4] M. K. Gospodarowicz, J. D. Brierley, and C. Wittekind, *TNM classification of malignant tumours*. Hoboken: John Wiley & Sons, 2017.
- [5] S. H. Cho *et al.*, "Essential Items for Structured Reporting of Rectal. Cancer MRI: 2016 Consensus Recommendation from the Korean Society of Abdominal Radiology," *Korean. J. Radiol.*, vol. 18, no. 1, pp. 132-151, 2017.
- [6] S. Trebeschi *et al.*, "Deep learning for fully-automated localization and segmentation of rectal cancer on multiparametric MR," *Sci. Rep.*, vol. 7, no. 1, p. 5301, 2017.
- [7] Y. LeCun, Y. Bengio, and G. Hinton, "Deep learning," *Nature*, vol. 521, no. 7553, pp. 436-444, 2015.
- [8] M. D. Zeiler and R. Fergus, "Visualizing and understanding convolutional networks," in *Computer Vision – ECCV 2014 European Conference on Computer Vision*, Cham, 2014, pp. 818-833: Springer.
- [9] A. Krizhevsky, I. Sutskever, and G. E. Hinton, "Imagenet classification with deep convolutional neural networks," in *Advances in Neural Information Processing Systems 25*, Red Hook, NY, 2012, pp. 1097-1105: Curran Associates.
- [10] K. Simonyan and A. Zisserman, "Very deep convolutional networks for large-scale image recognition," *arXiv preprint arXiv:1409.1556*, 2014.
- [11] C. Szegedy *et al.*, "Going deeper with convolutions," in *in: 2017 IEEE Conference on Computer Vision and Pattern Recognition (CVPR)*, New York, 2015, pp. 1-9: IEEE.
- [12] K. He, X. Zhang, S. Ren, and J. Sun, "Identity mappings in deep residual networks," in *in: Proceedings of the 2015 IEEE International Conference on Computer Vision*, New York, 2016, pp. 630-645: Springer.
- [13] G. Huang, Z. Liu, L. Van Der Maaten, and K. Q. Weinberger, "Densely connected convolutional networks," in *in: 2017 IEEE Conference on Computer Vision and Pattern Recognition (CVPR)*, New York, 2017, pp. 2261-2269: IEEE.
- [14] G. Litjens *et al.*, "A survey on deep learning in medical image analysis," *Med. Image Anal.*, vol. 42, pp. 60-88, 2017.
- [15] O. Ronneberger, P. Fischer, and T. Brox, "U-net: Convolutional networks for biomedical image segmentation," in *in: International Conference on Medical image computing and computer-assisted intervention*, Cham, 2015, pp. 234-241: Springer.
- [16] F. Milletari, N. Navab, and S.-A. Ahmadi, "V-net: Fully convolutional neural networks for volumetric medical image segmentation," in *in: Fourth International Conference on 3D Vision (3DV), 2016*, New York, 2016, pp. 565-571: IEEE.
- [17] J. Hagerly, R. J. Stanley, and W. V. Stoecker, "Medical Image Processing in the Age of Deep Learning," in *in: Proceedings of the 12th International Joint Conference on Computer Vision, Imaging and Computer Graphics Theory and Applications (VISIGRAPP 2017)*, 2017, pp. 306-311.
- [18] I. Goodfellow, Y. Bengio, A. Courville, and Y. Bengio, *Deep learning*. MIT press Cambridge, 2016.
- [19] S. Ioffe and C. Szegedy, "Batch normalization: Accelerating deep network training by reducing internal covariate shift," *arXiv preprint arXiv:1502.03167*, 2015.
- [20] I. J. Goodfellow, D. Warde-Farley, M. Mirza, A. Courville, and Y. Bengio, "Maxout networks," *arXiv preprint arXiv:1302.4389*, 2013.
- [21] N. Srivastava, G. Hinton, A. Krizhevsky, I. Sutskever, and R. Salakhutdinov, "Dropout: a simple way to prevent neural networks from overfitting," *J. Mach. Learn. Res.*, vol. 15, no. 1, pp. 1929-1958, 2014.
- [22] S. Ruder, "An overview of multi-task learning in deep neural networks," *arXiv preprint arXiv:1706.05098*, 2017.
- [23] P. Domingos, "A unified bias-variance decomposition and its application," in *in: Proc. 17th International Conf. on Machine Learning*, Burlington, 2000, pp. 231-238: Morgan Kaufmann.
- [24] J. Long, E. Shelhamer, and T. Darrell, "Fully convolutional networks for semantic segmentation," in *Proceedings of the IEEE conference on computer vision and pattern recognition*, 2015, pp. 3431-3440.
- [25] M. Drozdal *et al.*, "Learning normalized inputs for iterative estimation in medical image segmentation," *Medical Image Anal.*, vol. 44, pp. 1-13, 2018.
- [26] R. Srivaramangai, P. Hiremath, and A. S. Patil, "Preprocessing MRI Images of Colorectal Cancer," *International Journal of Computer Science Issues (IJCSI)*, vol. 14, no. 1, p. 48, 2017.
- [27] K. Zuiderveld, "Contrast limited adaptive histogram equalization," in *in: Graphics gems IV*, San Diego, 1994, pp. 474-485: Academic Press.

- [28] K. He, X. Zhang, S. Ren, and J. Sun, "in: Delving deep into rectifiers: Surpassing human-level performance on imagenet classification," in *Proceedings of the IEEE International Conference on Computer Vision*, Washington, 2015, pp. 1026-1034: IEEE Computer Society.
- [29] X. Glorot and Y. Bengio, "Understanding the difficulty of training deep feedforward neural networks," in *in: Proceedings of the Thirteenth International Conference on Artificial Intelligence and Statistics*, 2010, pp. 249-256.
- [30] D. P. Kingma and J. Ba, "Adam: A method for stochastic optimization," *arXiv preprint arXiv:1412.6980*, 2014.